Acta Materialia 231 (2022) 117919

Contents lists available at ScienceDirect

Acta Materialia

journal homepage: www.elsevier.com/locate/actamat

Solid-state dewetting of thin Au films on oxidized surface of biomedical TiAlV alloy

Aliya Sharipova[a], Leonid Klinger[a], Anuj Bisht[a], Boris B. Straumal[b], Eugen Rabkin[a,*]

[a] Department of Materials Science and Engineering, Technion – Israel Institute of Technology, Haifa 3200003, Israel
[b] Osipyan Institute of Solid State Physics of the Russian Academy of Sciences, Ac. Osipyan Str. 2, 142432 Chernogolovka, Russia

ARTICLE INFO

Article history:
Received 25 November 2021
Revised 23 February 2022
Accepted 31 March 2022
Available online 4 April 2022

Keywords:
Gold thin films
Nanoporous
Titanium alloy
Kinetics
Solid-state dewetting

ABSTRACT

Recent applications of solid-state dewetting for the functionalization of medical implants raise the question of the thin film dewetting kinetics on surfaces with natural roughness. In this work, we studied the initial stages of solid-state dewetting of thin nanocrystalline gold (Au) films deposited on an oxidized surface of a biomedical titanium-aluminum-vanadium (Ti-6Al-4V) alloy. The interrupted annealing technique was employed to study the evolution of holes in the film and film flattening. While a high number of dewetting holes was formed in the film at the early stages of dewetting at the temperature of 300°C, the nanoporous but continuous film morphology remained stable even after prolonged anneals at higher temperature of 500°C. We developed models describing Au thin film dewetting on surfaces with typical topographical features of oxidized Ti-6Al-4V. These models considered the Au diffusion along the grain boundaries as a controlling factor of the film flattening. The stabilization of nanoporous film structure was attributed to the slowdown of the dewetting holes expansion at the sharp edges of the substrate. Our work demonstrates that solid state dewetting of thin metal films deposited on the rough surface of oxidized metal can be utilized for producing continuous nanoporous metal coatings.

1. Introduction

Biofunctionalization of inorganic implant surfaces is one of the main goals in design of biomaterials and development of local therapies [1–3]. Surface biofunctionalization can be performed by modification of topography, introduction of bioactive coatings or fabrication of cavities/channels containing bioactive substances. Separately or combined, they can prevent intervention-induced infections, support cell adhesion and provide medical treatment. One of approaches to activate implant surface employs surface modification by gold (Au) or silver (Ag) nanoparticles (NPs). Surface modification by noble metal NPs leads to significant improvements in cell adhesion [4], promotion of soft tissue growth [5] and implant osseointegration [6].

Recently, several works reported the application of solid-state dewetting (DW) of thin films for fabrication of Au and Ag NPs on implant surface [7,8]. The phenomenon of thin films DW is well-known in the field of material processing in microelectronics, where it leads to device failure and is often undesirable. However, the DW can be utilized in cases where arrays of NPs are needed, such as decoration of biomedical surfaces. Indeed, DW process has several advantages over conventional techniques used to modify inorganic implant surfaces by noble metal NPs [6,9], namely: (1) it is non-destructive and provides good adhesion of NPs to substrate, (2) it is compatible with implants of different compositions, (3) it prevents NPs agglomeration, and (4) it enables an easy control over the NPs size. In details, poor wettability of the substrate by the film material is a necessary condition for DW. This condition is usually fulfilled for the metal films deposited on metal oxide substrates. In addition, in the context of implant surfaces, the surface oxide layer can serve as diffusion barrier preventing diffusion of the film material into the substrate during annealing/DW. Oxide films are always present on the surface of inorganic implants, either as a native oxide layer in metal-based implants or simply as an inherent part of the implant in ceramic-based implants. They can also be deliberately produced by oxidation or deposition. In latter case, their composition may differ from that of native oxide. Therefore, the solid-state DW for surface modification can be carried out on inorganic implants of different compositions, the only requirement being that they can withstand the heat treatment required for the DW. Size of NPs can be controlled by the thickness of the deposited film [10]. Also, the method can deliver ordered NPs having a very narrow controlled particle size distribution with the aid of thin film patterning during deposition [11]. In addition, the process is capable of providing NPs in a wide range of compositions, including two-phase NPs [12]. Finally, the process is scal-

* Corresponding author.
E-mail address: erabkin@technion.ac.il (E. Rabkin).

https://doi.org/10.1016/j.actamat.2022.117919
1359-6454/

able to accommodate fabrication of NPs at a broad spectrum of implant sizes thanks to advancements in thin film technology. The reported works on DW application for implant surface modification [7,8] confirmed the positive effects associated with the noble metal NPs. However, none of them have dealt with DW kinetics, an understanding of which is required for the rational design of NPs by the DW process.

Study of DW kinetics on implant surfaces should take into consideration surface morphology. Surface roughness inherent in implants significantly affects cell adhesion [13] and bacteria colonization [14]. To the best of our knowledge, only few works studied effect of surface patterning on thin film DW. Wang et al. have studies the DW of thin Au films on silica surface with inverted pyramids and circular holes patterns [15]. The possibility to form ordered Au NP arrays with mono- and bimodal particle size distribution was demonstrated, provided the thickness of the film is properly selected. The DW on surfaces with artificially created saw-tooth grating structures [16] and arrays of inverted pyramids [17,18] were investigated by Thompson and co-workers. They suggested a simple semi-quantitative model of DW on a patterned surface based on curvature-driven surface diffusion, assuming that the surface energy is isotropic [17]. However, the model reflected only evolution of the top surface of the film and did not accommodate interactions of the film with any part of the substrate surface [17]. In terms of practical applications, the ordered arrays of ferromagnetic cobalt (Co) NPs for possible data storage applications were produced by DW of thin Co films on a substrate with an ordered inverted pyramids pattern [19]. Jiang et al. have analyzed the kinetics of solid-state DW on curved substrates [20]. Unlike the others, they considered surface energy anisotropy and employed a thermodynamic variational approach to simulate the kinetics of the process [20]. In all works cited above the evolution of the metal films or particles on the surfaces with a simple periodic pattern has been considered. Such periodic roughness is atypical for surfaces of real materials. Moreover, none of these works addressed the contribution of grain boundary (GB) diffusion to DW kinetics, whereas it is known that thin films deposited on rough surfaces are polycrystalline or even nanocrystalline [17]. Therefore, kinetic model of DW process on surfaces with natural roughness should consider the GB diffusion together with the corrugated morphology of the substrate.

The aim of the present work is to understand the modalities of thin film DW on rough surfaces with natural topography. To reach this goal we performed combined experimental and modeling study of the solid-state DW of thin Au films deposited on the oxidized surface of medical Ti-6Al-4V alloy processed by mechanical grinding. The rest of the paper is organized as follows. In Section 2 we describe the experimental conditions of deposition and DW of Au thin film on the alloy surface and employed characterization methods. Section 3 is dedicated to the characterization of Ti-6Al-4V surface structure (Section 3.1), and the structure of as-deposited (Section 3.2) and dewetted Au films (Section 3.3). In Section 4, we discuss the obtained results and develop a kinetic model simulating solid-state dewetting of thin films on topographical features typical for the studied Ti-6Al-4V alloy. The results of this work are summarized in Section 5.

2. Materials and methods

2.1. Ti-6Al-4V sample preparation

For the investigations, the Ti – 6 wt.%Al – 4 wt.% V alloy (Ti-6Al-4V) of commercial purity has been used (VSMPO-AVISMA, Verkhnjaya Salda, Russia). The alloy is also known as VT6 according to Russian standard GOST 19807-91 [21]. The alloy was supplied as cold-wrought rod of 10 mm in diameter. The chemical composition of the samples verified with the aid of X-ray microanalysis in scanning electron microscope is presented in Table 1. The 1 mm thick discs have been mechanically cut from the rod. The obtained discs were sequentially ground with silicon carbide (SiC) abrasive grinding papers with grit sizes of 220, 400, 600, 600, 1000, 1200, and 2000.

Table 1
Chemical composition (wt.%) of the Ti-6Al-4V alloy studied in the present work.

Element	Al	V	Zr	Ti
GOST 19807-91	5.3–6.8	3.5–5.3	<0.3	Balance
Actual VT6 samples	5.97±0.37	3.87±0.37	Not detected	Balance

Samples were oxidized at 740 °C for 30 min in the ambient air to increase the thickness of the surface oxide film and to modify surface roughness. Oxidation conditions were chosen based on reported data on Ti oxidation [22]. We aimed to obtain a single-phase titanium oxide (TiO_2, rutile) to minimize possible influence of substrate composition on subsequent Au deposition and dewetting.

2.2. Au film preparation and dewetting

Electron beam deposition (Airco Temescal BJD 1800) was employed to deposit a 50 nm thick Au film on the oxidized Ti-6Al-4V samples. Prior the deposition, Ti-6Al-4V samples were cleaned in ultrasound baths of acetone, methanol and isopropanol, in the given sequence. Deposition of the film was performed in a vacuum chamber with a base pressure of 4.7×10^{-7} Torr at room temperature at a rate of about 1 Å/s.

The as-deposited Au films were annealed in a rapid thermal annealing furnace (RTA: ULVAC-RIKO MILA-5000-P-N) in the flow of forming gas (Ar + 10% H_2, 99.999% purity) to avoid Ti-6Al-4V samples oxidation simultaneously with solid-state DW. The heating rate was 40°C/s, which was followed by an isothermal annealing for the required time. Thermal treatments were performed at 300 °C for interrupted time intervals 5, 5, 15 and 30 min, corresponding to cumulative annealing times of 5, 10, 25 and 55 min. Additional long-time annealing was performed at 300 °C for 2 h and then at 500 °C for 2 h.

2.3. Characterization methods

The average chemical composition of the alloy samples was verified using scanning electron microscopy (SEM) and X-ray microanalysis with a Tescan Vega TS5130 MM instrument (Tescan Orsay Holding a.s., Brno, Czech Republic) equipped with an energy dispersive spectrometer INCA Energy 450 (Oxford Instruments Industrial Ltd., Abingdon, Oxon, UK). Phase composition of the oxidized Ti-6Al-4V samples was characterized by X-ray diffraction using CuK_α radiation with parallel beam optics (XRD; Rigaku SmartLab 9kW). A filter was employed to eliminate the contribution from K_β components from source during measurements. X-ray diffraction measurements were performed in θ–2θ mode with 20 deg $\leq 2\theta \leq$ 80 deg with a scan step of 0.1 deg and scan rate of 1 deg/min. Diffraction patterns were compared with the references in the ICDD database for phase identification. The morphology and microstructure of Au films were characterized by high-resolution field emission scanning electron microscopy (HR SEM; Carl Zeiss AG – Ultra Plus) equipped with backscattered electron (ESB), secondary electron in-lens (InLens), and secondary electron type II (SE2) detectors. The surface topography of samples was studied by atomic force microscopy (AFM; Park Systems XE-70) in a tapping mode. The topography images were corrected using Flattening tool (Entire region option) in XEI software. The same software was employed to determine the roughness of surface regions of 10×10

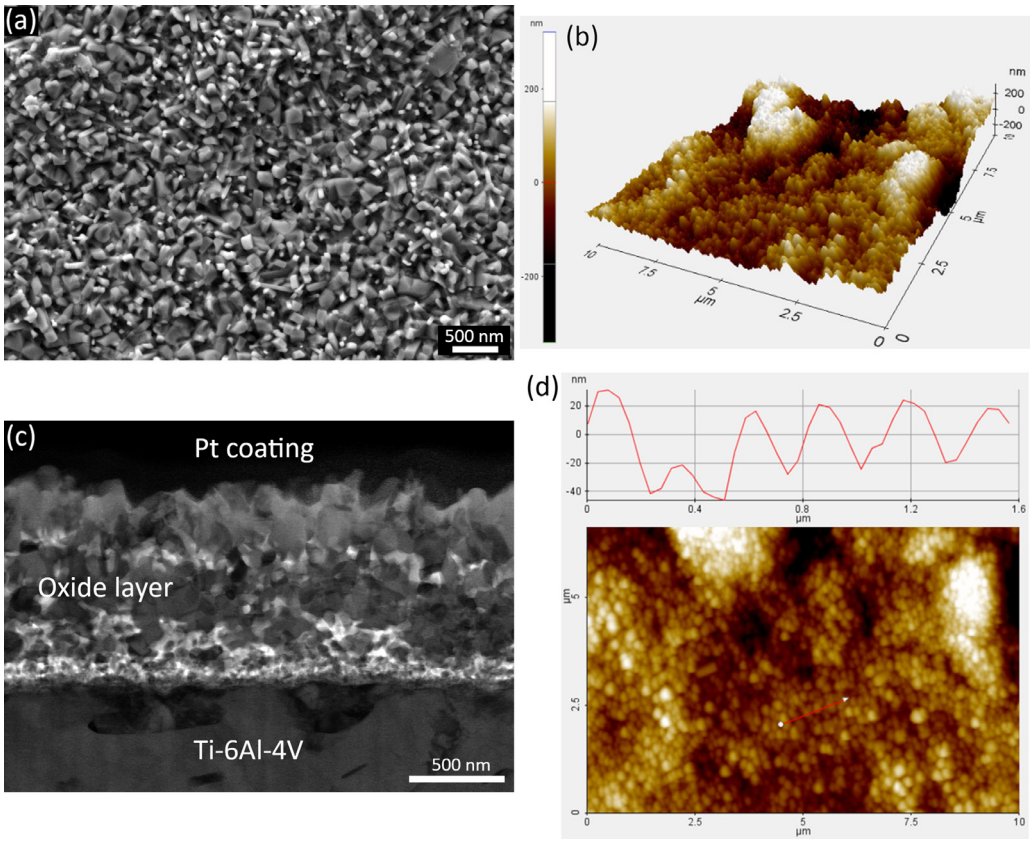

Fig. 1. Ti-6Al-4V oxidized in air at 740 °C for 30 min: (a) HR SEM (SE2) micrograph, (b,d) AFM image of the surface and typical line topography profile, and (c) STEM DF2 micrograph of the cross-section

µm^2 in size. Further, in-depth microstructural characterization of the interface between the Au film and oxide was carried out on the cross-sectioned transmission electron microscopy lamellae of selected samples prepared by the lift-off method in dual focused ion beam system (FIB; FEI Helios NanoLab). FEI Helios NanoLab system equipped with through the lens detector (TLD) was also utilized for HR SEM imaging of selected samples cross-sections. The local microstructural and chemical characterization were carried out using aberration-corrected transmission electron microscope (TEM; FEI Themis G2) operating at 300 keV. TEM micrographs and energy dispersive spectroscopy (EDS) maps were recorded in the scanning transmission electron microscopy (STEM) dark field (DF2 and DF4), high-angular annular dark field (HAADF) and bright field (BF) modes. A 94 mm working camera length was chosen during the STEM imaging. Corresponding collection angles for various detectors were 91–200 mrad for HAADF, 22–85 mrad for DF4, 12–19 mrad for DF2 and 9 mrad for BF.

3. Results

3.1. Morphology and structure of the oxidized Ti-6Al-4V surface

Surface of the oxidized Ti-6Al-4V sample was characterized employing HR SEM and AFM. HR SEM image showing surface of the medical alloy after oxidation is given in Fig. 1a. The as-formed oxide layer was composed of nanoscale crystals forming naturally corrugated surface. In the following, the terms “natural roughness” or “natural topography” are used to describe the naturally occurring roughness of the oxidized alloy surface, as opposed to the artificially designed (patterned) roughness investigated in the works of Giermann and Thompson [16,17]. AFM image of the 10 × 10 μm^2 region presented in Fig. 1b unveils that the formed oxide crystals are typical for the entire surface of the sample. They grow on nanoscale scratches, as well as on inclined surfaces of microscale hills and pits of the as-prepared Ti-6Al-4V. Shallow structure of hills and pits shows no effect on the direction or structure of the grown crystals (Fig. 1b, Fig. S1 in *Supplementary Material*). HAADF STEM micrograph shows that they are oriented in different directions, form nanoscale buttes and various types of pits in between (Fig. 1c). We should note that corrugated oxide films are typical for oxidized Ti and Ti alloys and were described in details previously [23,24].

To determine typical topographical features of the oxidized surface, we examined the cross-sectional STEM images (Fig. 1c) and surface line topography profiles obtained from the AFM micrographs (Fig. 1d). Here we have described a typical single line topography profile due to the random orientations of the grown crystals resulting in large variety of buttes and pits. Averaging approach for surface analysis in this case would diminish typical shape of pits and hills. Dimensions of the crystals are in a range of 50–200 nm (Fig. 1). Pits between them are of the same size range, however, random orientations of grown crystals results in a large variety of pit shapes. Majority of pits have a shape of inverted pyramids tapered to an acute angle at the bottom. The longitudinal cross-section of those pyramids is an inverted triangle with an acute apex (Fig. 1c,d). Therefore, at the later stage we will employ a shape of inverted triangular prism to describe these features in the kinetic modeling (Section 4.2).

The presence of two distinct phases in the bulk of metallic alloy is evident in the STEM DF2 micrograph (Fig. 1c). Moreover, the oxide layer is composed of multiple oxide phases. The XRD spectrum and cross-sectional STEM images of the oxide layer shedding light on its composition and structure are presented in Fig. 2. XRD spectrum of the as-prepared Ti-6Al-4V (Fig. 2a) shows a presence

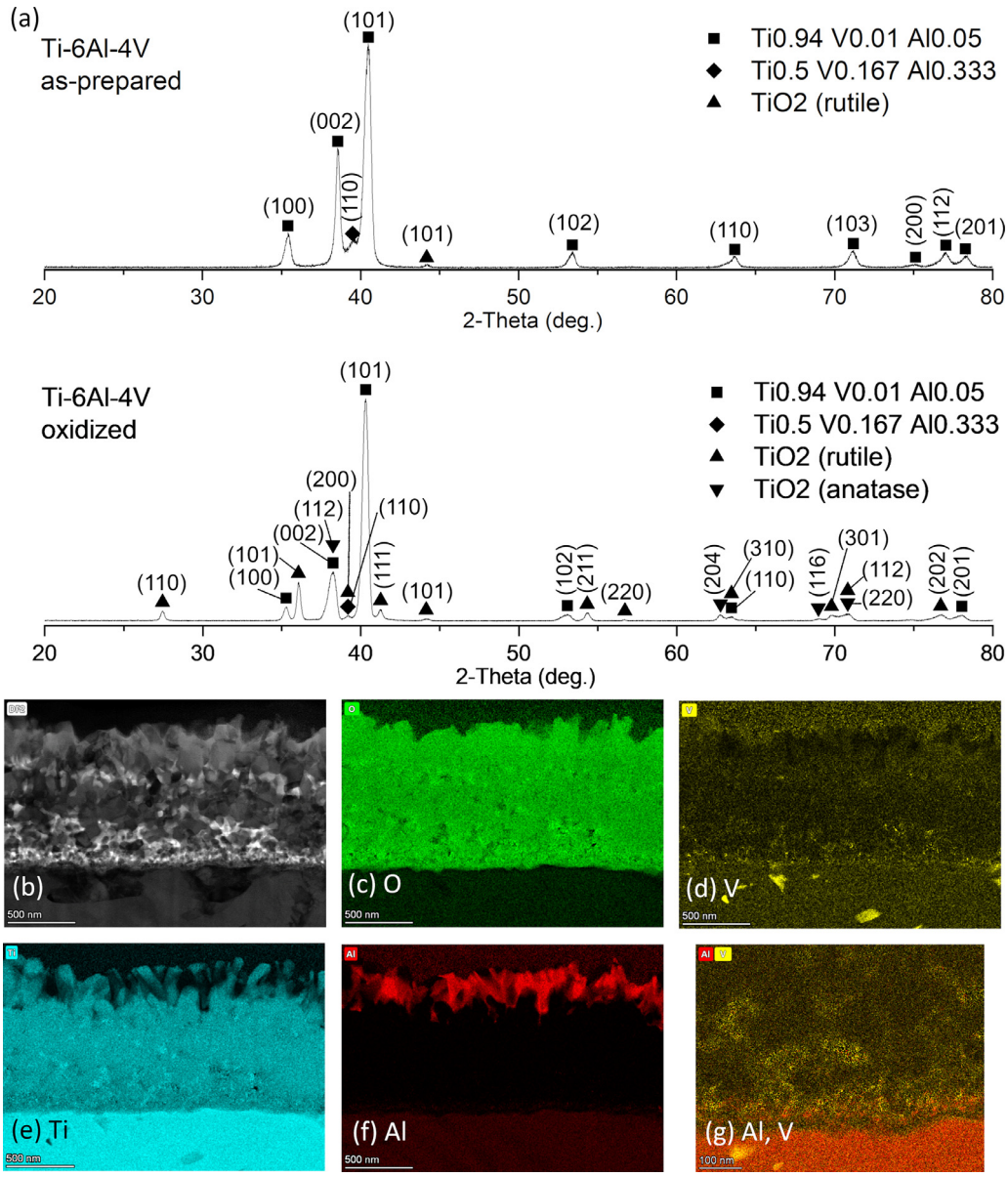

Fig. 2. Ti-6Al-4V oxidized in air at the temperature of 740 °C for 30 min: (a) XRD spectrum, (b) STEM DF2 micrograph of the cross-section with elemental maps of (c) O, (d) V, (e) Ti, (f) Al, and (g) Al and V.

of two phases in the bulk of the titanium medical alloy: $Ti_{0.94}$–$V_{0.01}$–$Al_{0.05}$ (ICDD 04-020-7055) and $Ti_{0.5}$–$V_{0.167}$–$Al_{0.333}$ (ICDD 04-015-2203), along with TiO_2, rutile (ICDD 00-002-0494). Chemical compositions of the identified phases are in good agreement with the chemical composition of Ti-6Al-4V samples determined by X-ray microanalysis in SEM (Table 1). While rutile is a primary oxide in the native and grown oxide layers, another TiO_2 phase, anatase (ICDD 00-021-1272), formed during the oxidation. To understand whether the different oxide phases also differ in composition, we performed EDS STEM analysis of the oxide layer cross-section (Fig. 2b). STEM DF2 micrograph of the investigated region is shown in Fig. 2b along with O, V, Ti and Al EDS elemental maps (Fig. 2c-f). The thickness of oxide layer is about ~900 nm (Fig. 2c). Unlike the uniform native oxide layer, the oxide layer in oxidized sample consists of multiple oxides roughly distributed in three layers (Fig. 2). The oxide layer has small pores. The outer most surface oxide layer consists of two phases: Ti oxide (Fig. 2e) and Al oxide (Fig. 2f). The middle oxide layer has a relatively uniform composition, nonetheless it is deficient in Al. The bottom oxide layer adjacent to the alloy bulk consists of large and small grains rich in Al and V (Fig. 2g), with smaller grains adjacent to bulk. This is the oxide layer without atomic segregation. Overall, the oxidation process resulted in segregation of Al atoms in the topmost layer. Such layered structure of Ti-6Al-4V oxide film is typical for selected oxidation conditions and was previously described by Du et al. [24]. At the same time, Al oxide (Al_2O_3) on the top of the oxide layer is not detected in the XRD spectrum (Fig. 2a). This is probably because a low volume fraction of nanoscale Al_2O_3 (Fig. 2f) results in small and broad diffraction peaks that could not be distinguished from the background. Alternatively, the amorphous structure of the formed Al_2O_3 and misalignment with the incidence angle could make detection of the Al_2O_3 phase difficult. Moreover, the peaks of the two metallic Ti-6Al-4V phases and rutile partially overlap with the peaks of various Al_2O_3 phases. It should be noted that significant enrichment by Al near the oxide/gas interface of the Ti-6Al-4V alloy (similarly oxidized at 600–700 °C) was detected by Frangini et al. [25] employing EDX microanalysis, whereas no or weak XRD signals of Al_2O_3 were reported. It should be noted that for DW it

is of minor importance whether the primary phase of the oxide layer in contact with Au is rutile (TiO_2) or alumina (Al_2O_3). This is because of close values of Au-substrate adhesion energies and resulting similarity in the contact geometries at the Au-substrate-ambient contact line [26,27]. Therefore, in what follows, we will consider rutile (TiO_2) as a substrate material in the modeling of DW kinetics on a corrugated substrate.

3.2. Morphology and structure of the Au film deposited on the oxidized Ti-6Al-4V

The HR SEM micrographs of oxidized Ti-6Al-4V with deposited thin Au films are presented in Fig. 3. HR SEM image of the Au thin film on the oxidized Ti-6Al-4V sample (Fig. 3a) shows an apparent homogeneously covered surface of the sample. However, the top-view micrograph does not provide the full picture of the film morphology and microstructure. The cross-sectional HR SEM micrographs demonstrate that Au film deposited on the oxidized Ti-6Al-4V sample exhibits inhomogeneous coverage. This inhomogeneity results from the shadowing effect from the "inclined" oxide grains during the Au deposition (Fig. 3b). In many cases, discontinuities/holes in the as-deposited film contain ultrafine Au nanoparticles (Fig. 3b, arrow). Shadowing effect also leads to the variations of film thickness in the adjacent areas. At the same time, homogeneously deposited film is presented in the regions with low roughness or on the oxide grains grown "normally" to the surface (Fig. 3b,c). In those areas, the film is homogeneous in thickness, and it well replicates the roughness of the underlying oxide layer. It is worth noting that cone-shaped pits of the oxidized surface with obtuse cone angles are well covered with Au (Fig. 3c, arrows).

3.3. Characterization of the Au film dewetting on oxidized Ti-6Al-4V

HR SEM images of Au film deposited on oxidized Ti-6Al-4V alloy after 5-min annealing at 300°C are presented in Fig. 4. Significant grain growth occurred in the film after 5-min annealing (Fig. 4a). Numerous big and irregularly shaped holes are formed in the film at substrate pits between large oxide grains. However, hole's rims have rounded, symmetrical shape with no elevation or tortuosity. At some areas, the film does not fully break down leaving irregularly shaped islands (Fig. 4a). These contiguous islands contain small holes similar to those observed during initial dewetting stages of the thin film deposited on a flat substrate. Cross-section images of these islands confirm that the film remains continuous in substrate regions with low roughness (Fig. 4c). Nonetheless, additional thinning of thin connecting film region is observed (Fig. 4c). Big holes in the film form at substrate pits between protruding crystals (Fig. 4b, arrows; Fig. 4d). Steeply inclined walls of such crystals have Au nanoparticles attached to them (Fig. 4d, arrowheads); these nanoparticles result either from the discontinuity of the initially deposited film (Fig. 3b), or from the film retraction during the annealing.

Film on oxidized Ti-6Al-4V starts to flatten after 5 min annealing (Fig. 4a). This transformation is more visible at contiguous island of the film (Fig. 4c), though similar film behavior is observed on relatively flat top regions of the oxide film encompassing large oxide grains of comparable heights (Fig. 4d). First, the exterior surface of the Au film does not well replicate the surface roughness of the oxidized alloy. Consequently, dewetted film is uneven in thickness with thicker film at substrate pits and thinner film at protruded parts of the substrate (Fig. 4c, line segments). Lastly, we observed pores and convex interior surface of the Au film in sharp pits (Fig. 4c, arrow). Since similarly-shaped pits are fully filled with Au in the as-deposited film (Fig. 3c, arrows), the phenomena of the film retraction from the small narrow pits is referred to as film flattening. Retracted film also leaves nanoparticles on the bottom of the pit (Fig. 4c, arrowheads). Nonetheless, film flattening after 5 min annealing is insignificant and cuboidal grain morphology of the underlying oxide substrate is clearly distinguishable (Fig. 4a). Following annealings for 10 min and 25 min (cumulative times) result in a similar structure of the film, which exhibits regions retracted from the sharp pits with Au nanoparticles left in the bottom (Fig. S2 in *Supplementary Material*).

Longer annealing (cumulative time of 55 min) leads to pronounced film flattening and increased frequency of smaller holes (Fig. S3 in *Supplementary Material*). To validate film flattening, we performed STEM investigation of a representative cross-section region (Fig. 5). These micrographs and their scheme (Fig. 5b) clearly validate film retraction from the sharp pits and its relation to the flattening phenomenon. We also performed EDS analysis of the pit region with nanoparticles from which the deposited Au film has retracted to determine the nanoparticles composition. STEM DF4 micrograph is shown in Fig. 5a along with Au, O, Ti, Al elemental EDS maps (Fig. 5b-f). The DF4 micrograph (Fig. 5a) confirms polycrystalline nature of the Au film on the polycrystalline Ti oxide (Fig. 5b), with evidence for the presence of twins (Fig. 5c-f). The presence of distinct Ti (Fig. 5d) and Al (Fig. 5e) oxide grains on the outer surface of the oxide layer in contact with Au film is evident. The nanoparticles present at the bottom and on the walls of the pit are identified to be Au nanoparticles (Fig. 5c). STEM EDS analysis (Fig. 5c-e) further unveils that the retraction of Au film is independent on composition of substrate oxide. In this image, the wall of one of the pits (left, small) consists of Ti and V oxides, while another pit (central, big) has Ti, V oxides on the left side and Al oxide on the right side (Fig. 5d,e). Regardless of the composition, Au film retracts from both pits leaving Au nanoparticles at the bottom (Fig. 5c). Therefore, we conclude that film retraction is driven by topographical features of the substrate rather than differences in its composition. Based on that and aforementioned XRD analysis (*Section 3.1*, Fig. 2a, oxidized Ti-6Al-4V), we consider TiO_2 (rutile) as a substrate material in our model.

In order to examine advanced stages of the process, we performed additional heat treatments for 2 h each at 300 °C and then at 500 °C. SEM micrographs acquired after consecutive annealings are summarized into morphology map highlighting the initial and advanced stages of the process (Fig. 6). It is clear that as-deposited film follows the complex cuboidal topography of the oxidized Ti-6Al-4V. The film after long-time annealing is flattened, making impossible to track the shape of the corrugated surface underneath. Grains in the film after long-time annealing are coarser than in the as-deposited state, which was confirmed by the narrowing of Au peaks in the XRD spectra (Fig. S4 in *Supplementary Material*). The film after long-time annealing exhibits a porous structure with no signs of typical DW, i.e., formation of separated film islands and nanoparticles.

In addition, we investigated a region with a film thickness gradient caused by the shadowing effect from the holding pin during the Au deposition. Fig. 7 presents SEM micrographs of the region with the Au film thickness gradient after long-time annealing. The bright contrast of the Au film/NPs in the images acquired by the ESB detector (Fig. 7, low-resolution micrograph) enabled us to estimate the initial thickness of the film in different regions, assuming a linear thickness gradient from 50 nm to 0 nm (Fig. 7, triangle scheme). Obtained HR SEM micrographs (SE detector) clearly show that the DW on naturally corrugated surfaces depends on film thickness and most probably on the size of the rough surface features. The acquired SEM micrograph of the surface without deposited film (Fig. 7, no Au film) shows no change in the structure of the oxidized Ti-6Al-4V after performed long-time annealing, which confirms film flattening on the cuboidal topography of the substrate (Fig. 6).

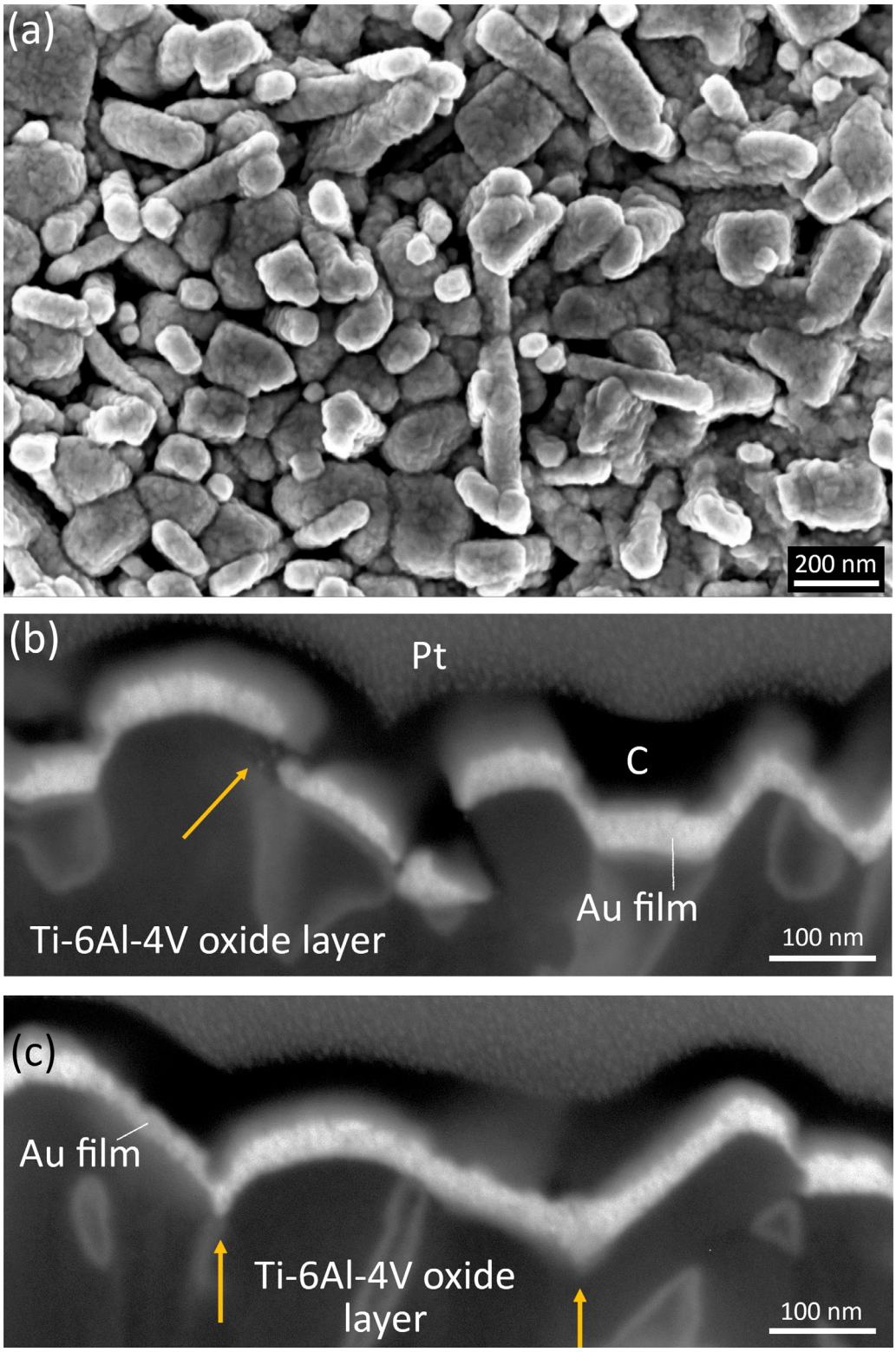

Fig. 3. HR SEM (TLD) micrograph of Au film deposited on oxidized Ti-6Al-4V: (a) surface (top view), and (b,c) cross-section. Pt and C are the platinum and carbon protective FIB coatings, respectively.

Nonetheless, regions with estimated thickness of less than 10 nm show typical thin film DW with formation of separated islands and nanoparticles (Fig. 7). In these cases, most likely, the as-deposited film does not reach percolation threshold for the present substrate roughness. Therefore, each facet of the oxide cuboids acts as a separate flat substrate where typical thin film DW is observed. Similar results on the effect of TiO_2 surface roughness on the DW kinetics of Au thin films were recently reported by Striubas et al. [28]. They observed that surface roughness starts playing a predominant role in NPs formation in Au films of initial thicknesses of 10 and 15 nm.

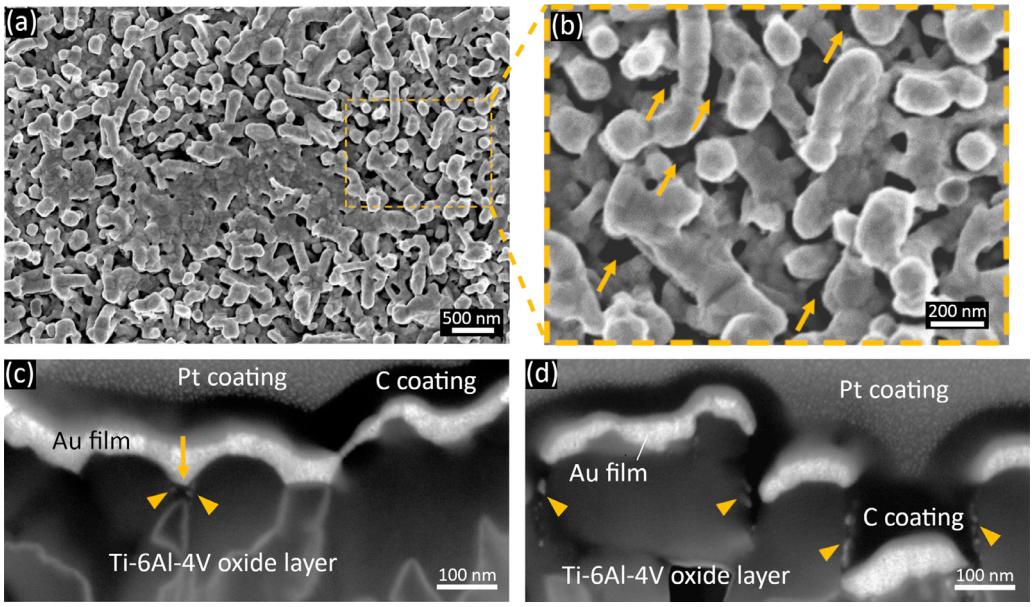

Fig. 4. HR SEM (TLD) micrograph of Au film deposited on oxidized Ti-6Al-4V after annealing at 300°C for 5 min in forming gas: (a,b) surface (top view), and (c,d) cross-section. Pt and C are protective FIB coatings.

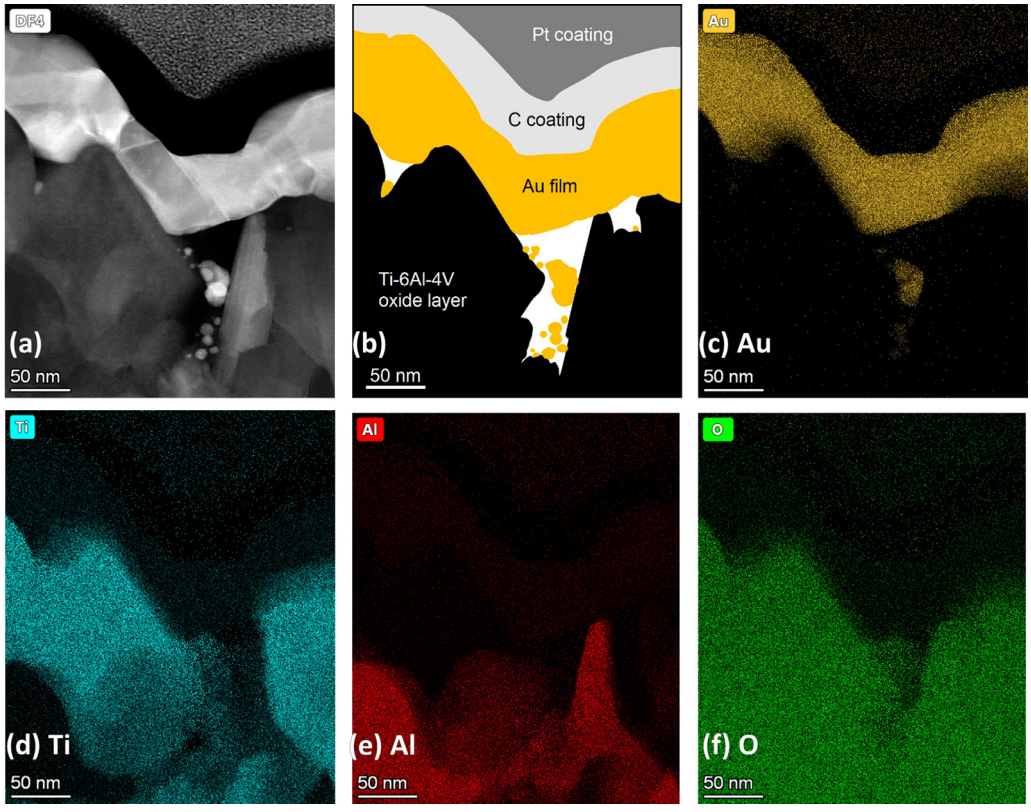

Fig. 5. STEM EDS micrograph of Au thin film on oxidized Ti-6Al-4V after annealing at 300 °C for 55 min in forming gas: (a) STEM DF4 micrograph with (b) its scheme and elemental maps of (c) Au, (d) Ti, (e) Al, and (f) O.

4. Discussion

4.1. General features of dewetted films on surfaces with natural roughness

Our goal was to determine modalities of solid-state DW of thin films on surfaces with natural roughness. Our findings suggest that initial stage of thin film DW on surfaces with natural roughness is similar to the one on flat surfaces, especially with regard to holes formation (Fig. 4). Moreover, the stage of holes/pores formation is accelerated by films thickness inhomogeneity resulting from the shadowing effect during the deposition (Fig. 3b). However, the following stages of the process on the surfaces with natural roughness deviate from those of thin films DW on flat surfaces. Our findings show that long-time annealing of thin film on naturally corrugated surfaces does not lead to formation of isolated islands

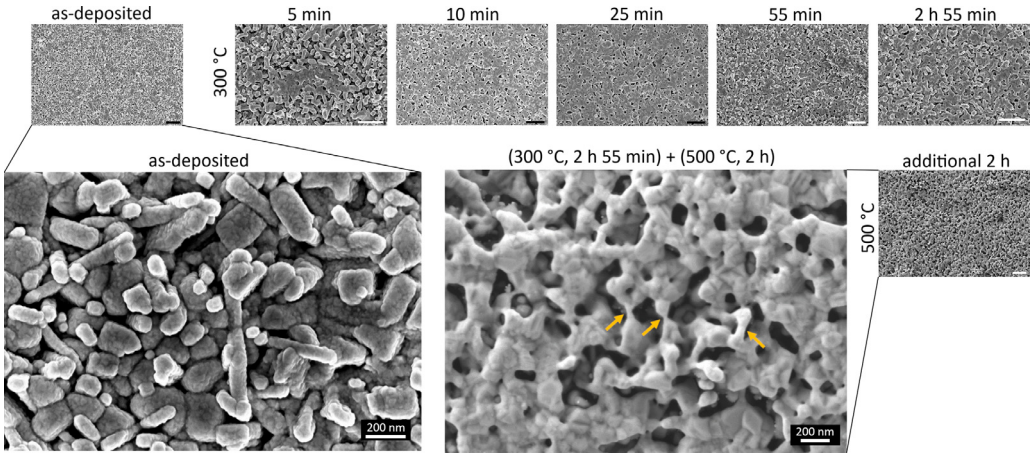

Fig. 6. Morphology maps of Au thin film on oxidized Ti-6Al-4V in the as-deposited state and after several consecutive annealings. Denoted time corresponds to cumulative annealing time. Unannotated scale bars correspond to 1 μm.

and nanoparticles, but to a flattened nanoporous film (Figs. 5, 6). At the same time, formation of nanoparticles on highly corrugated surfaces, i.e., typical result of thin film DW, is possible for ultra-thin films (Fig. 7).

Initial stage of Au thin film DW on Ti-6Al-4V with natural topography is very similar to that for Au thin film DW on flat TiO_2 reported in work of Schaaf and co-workers [29], as well as other works on Au thin films DW on flat surfaces [30–32]. There, the initial stage of DW (continuous films of 25 nm to 50 nm thickness) is characterized by holes formation. As expected, in this work the presence of rough features on substrate surface facilitates formation of holes. Rough features imply thickness inhomogeneity and holes in the as-deposited films, which increase film instability. We can qualitatively assess the influence of surface roughness by comparing results obtained in this work with results of Au thin film DW on flat TiO_2 reported in work of Schaaf et al. [29]. Although, there Au film was thinner (20 nm), noticeable number of holes formed only after heat treatment for 30 min at the same temperature of 300°C. In our work, a thicker film (50 nm) on a very rough surface of oxidized Ti-6Al-4V becomes holey after annealing for 5 min at 300 °C (Fig. 4). Moreover, density of holes observed in the present work after 5 min annealing is significantly higher than that in the 20 nm-thick Au film on flat TiO_2 after longer annealing for 30 min at higher temperature (400°C) [29]. Primarily, the holes can be found between the rough features and protruded oxide crystals; they grow from the preexisting holes or thinner areas in the as-deposited film (Fig. 3b). Symmetrical and rounded shape of the holes is similar to the one reported at initial DW stage of Au film deposited on flat TiO_2, when holes just nucleate [29]. These results show that higher surfaces roughness leads to lower stability of the as-deposited thin film.

Surprisingly, subsequent annealing of the Au film deposited on oxidized Ti-6Al-4V does not follow the path of Au DW on flat TiO_2 [29]. Next stage of the Au thin films DW on flat substrates is characterized by the holes growth and development of porous film until holes impingement and formation of separate islands [30–32]. Instead, during the DW of Au thin film on the corrugated surface we detect holes shrinking, increasing of holes area density, and film flattening. The porosity of partially dewetted Au films on flat surfaces is dendritic and tortuous, with columnar structure of holes [30–32]. On the contrary, partially dewetted Au film obtained in the present work is characterized by densely spaced round symmetrical holes (Fig. 6). The overall film morphology is essentially three-dimensional, containing flattened sections bridging the pores (Fig. 5) and suspended necks (Fig. 6, arrows), which have not been reported for Au thin films DW on flat surfaces. This behavior resembles the superhydrophobicity of rough hydrophobic surfaces wetted by water (Lotus effect) well-known in the classical theories of liquid-phase wetting [33]. The phenomenon of thin film flattening on surfaces with designed roughness was previously reported by Giermann and Thompson [17]. They demonstrated that 60 nm-thick Au film deposited on an array of inverted pyramids of 140 nm in depth patterned on oxidized Si wafer flattens and withdraws from the pits after annealing at 600 °C for 15 min. Longer annealing resulted in full DW, with all Au cleared of the pits. The authors developed a model of film flattening controlled by curvature-driven surface diffusion. Such model was useful in prediction of morphologies of fully dewetted films, yet it did not capture the kinetics of film flattening, because the surface diffusion alone cannot ensure the film withdrawal from the pits. Though the results of the present study for short annealing times are consistent with the findings of Giermann and Thompson (film flattening and nucleation of pores), the long-time annealing does not result in full film DW. Instead, the film continues to flatten, and the porous structure is stabilized (Fig. 6). Thus, we conclude that the model suggested in Ref. [17], which considers surface self-diffusion driven by the gradient of local surface curvature as a sole mechanism of the film DW, is not sufficient to explain experimental results of the present work.

In what follows we will formulate a model of the DW of thin film deposited on substrates with topographical features typical for the surfaces with natural roughness. Like in the study of Giermann and Thompson, we will consider curvature-driven surface diffusion as a main mechanism of the mass transfer, yet we will explicitly take into account the effect of GBs on the film topography and kinetics of mass transfer.

4.2. A model of the thin film dewetting on surfaces with natural roughness

We model evolution of the external surface of the film affected by the presence of GBs supposing that that main mechanism of the mass transfer is surface diffusion. The GB diffusion will be taken into account while considering the film flattening. All configurations are two-dimensional. The surface diffusion equation is solved numerically employing the method proposed by Dornel et al. [34]. The details of the model are presented in *Supplementary Material*. The following values of relevant parameters were employed in calculations: $D_s = 1.5\times10^{-15}$ m^2/s [35], $\nu_s\Omega = 5\times10^{-10}$ m, $\Omega = 1.685\times10^{-29}$ m^3/at, $\gamma = 1.4$ J/m^2 [36], $T = 573$ K, where D_s, ν_s, Ω and γ are the surface self-diffusion coefficient of Au, the number of mobile surface atoms per unit area of the surface,

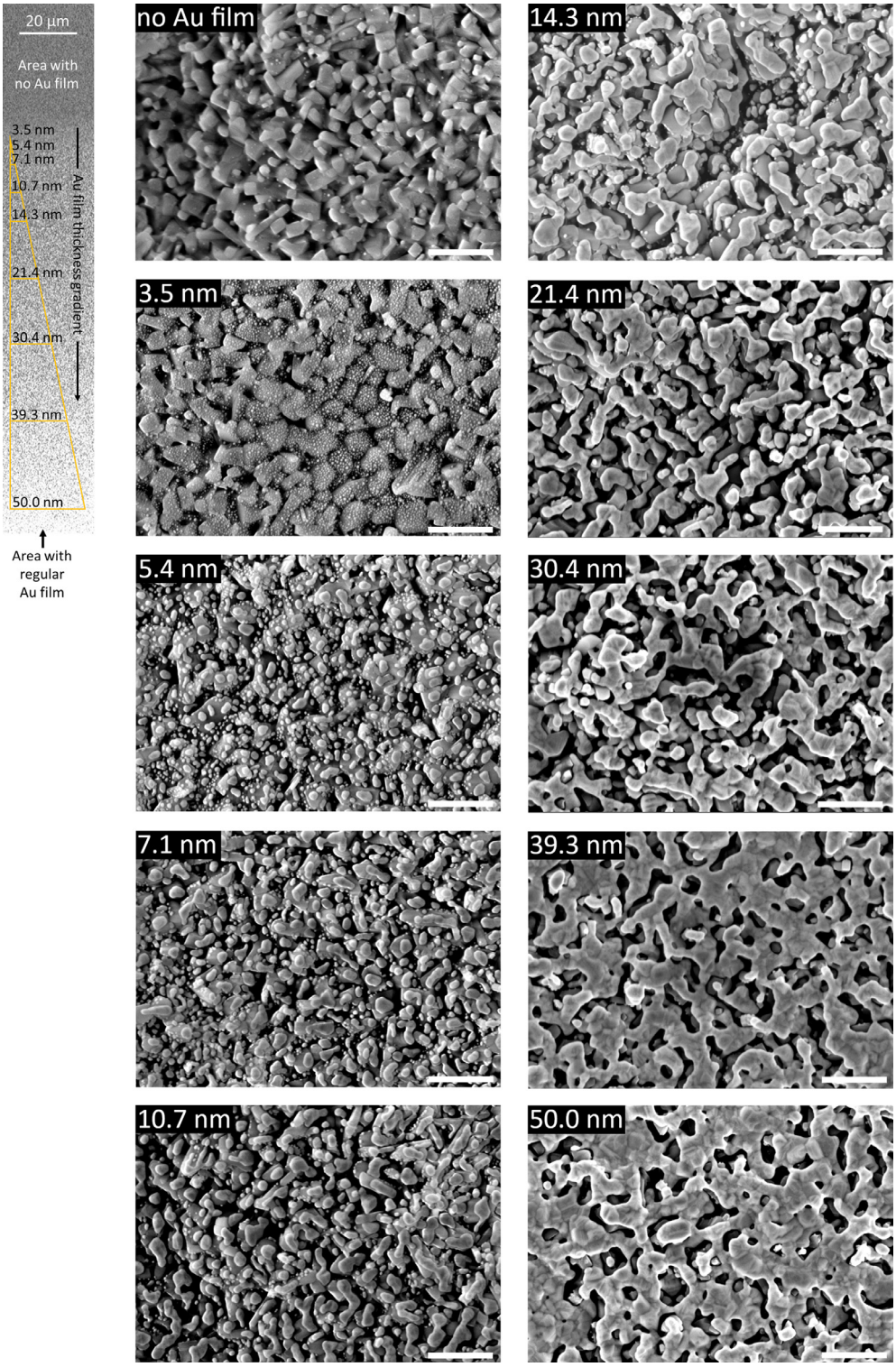

Fig. 7. Morphology maps of Au thin film with thickness gradient on oxidized Ti-6Al-4V after long-time annealing. Left low-resolution micrograph acquired by ESB detector represents thickness gradient due to shadowed Au deposition. Triangle scheme reflects thickness gradient of Au thin film. HR SEM micrographs show structure of the dewetted Au film with different initial thicknesses. Estimation of initial film thickness is based on assumption of linear thickness gradient from 50 nm to 0 nm. The scale bar is 500 nm.

atomic volume of Au, surface energy of solid Au, and the temperature of the experiment, respectively.

Concerning the surface self-diffusion coefficient in Au, there is a wide scatter of available literature data on the corresponding Arrhenius parameters, leading to high uncertainty in the value of diffusion coefficient extrapolated to the temperature of 300°C. For example, the data of Goebel and von Blanckenhagen yield the surface self-diffusion coefficient of 1.5×10^{-15} m^2/s [35], whereas the correlation of Gjostein for a number of metals with face-centered cubic (FCC) lattice yields a value of 1.1×10^{-12} m^2/s [37]. We found that the former value obtained from the kinetics of flattening of the AFM-modified surface of Au results in a better agreement between

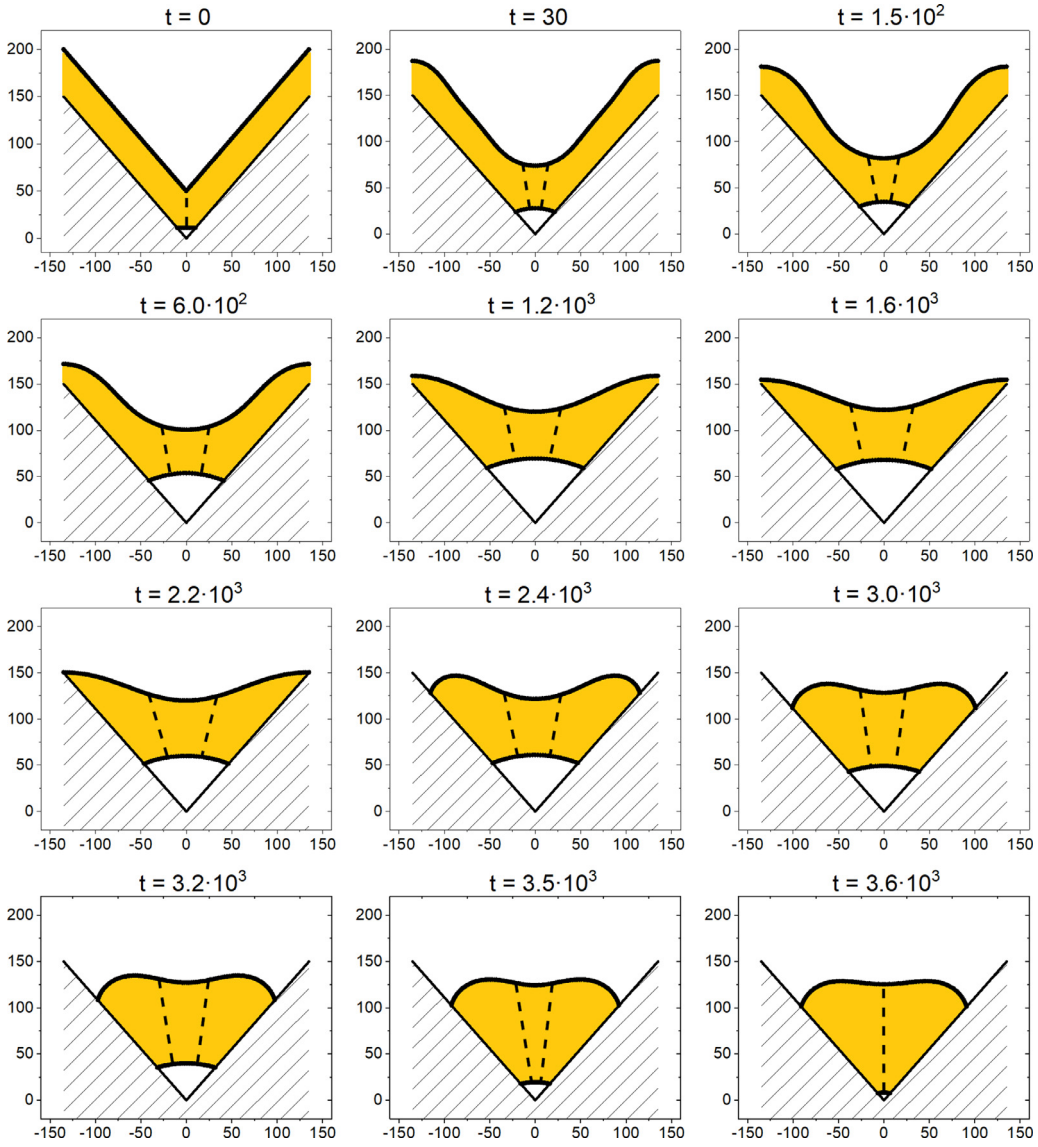

Fig. 8. A cross-section showing evolution of the film in the pit over time (t, s); dimensions are in units of nm. Positions of GB (dashed lines) are representative.

the experiment and simulations, and adopted it in all further calculations.

4.2.1. Au film flattening on the surface of oxidized Ti-6Al-4V samples

Let us consider a surface unit with a prismatic groove mimicking the natural roughness of the oxidized Ti-6Al-4V sample (see Fig. 8). We will assume that a small initial "seed" pore of width w is present at the bottom of the groove, but otherwise the Au film conformally fills the rest of the groove, repeating its morphology. We will describe the evolution of both external surface of the film and surface of the pore using the method of Dornel et al. [34], adding to this description an additional mass transfer from the surface of the pore to external surface of the film by the GB diffusion. The GB diffusion flux, J_{gb}, is given by

$$J_{gb} = \frac{D_{gb}\nu_{gb}}{kT}\frac{\bar{\mu}_p - \bar{\mu}_s}{\bar{h}_{ps}}m, \tag{1}$$

where $\bar{\mu}_p$, $\bar{\mu}_s$ and $\bar{h}_{ps}$ are the average chemical potentials on the surface of the pore, on the external surface, and an average distance between these surfaces, respectively, the latter two parameters are calculated for the section of external surface of the width w located above the pore; m is number of the GBs connecting the surfaces (this model enables an arbitrary number of GBs in one cell, dashed lines in Fig. 8). Since the GBs can move during annealing, the parameter m is considered as an average number of GBs above the pore during the whole duration of annealing. Due to the same reason (GB migration) we do not consider the GB grooving here, formally assuming zero GB energy. The positive grain boundary flux leads to the pore expansion. During the time dt the upward pore surface displacement is

$$\delta Y = \Omega\frac{J_{gb}}{w}dt \tag{2}$$

The central section of the external surface (of the width w) is then shifted on the same distance δY. We have employed the following value of the GB diffusion coefficient: $D_{gb} = 1.6\times10^{-13}$ m^2/s [38], and assumed $m = 4$ for illustrative purposes. We also assume the zero-flux condition at the termini of simulation cell, which means that the initial configuration in Fig. 8 represents one unit in a periodic arrangement of grooves. The chemical potential of Au atoms at the contact point between the film and the substrate is calculated by infinitesimal displacement of the contact point along substrate and determining the concomitant change of energy of all

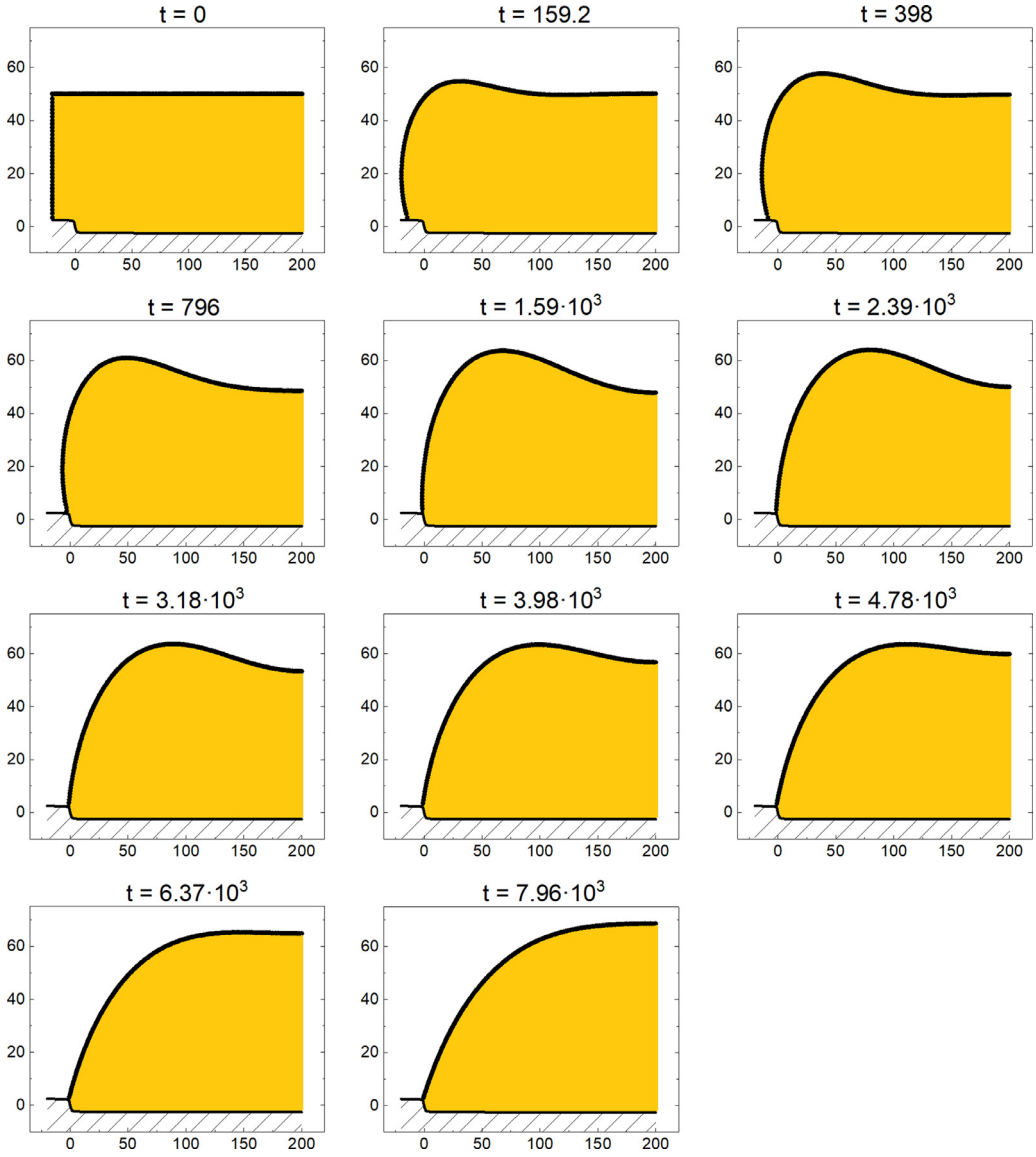

Fig. 9. A cross-section showing evolution of the film deposited on a substrate with a sharp step over time (t, s); dimensions are in units of nm.

surfaces and interfaces. To this end, the equilibrium value of the contact angle, θ_c, of solid Au on the TiO_2 surfaces is needed. We adopted the value of the contact angle $\theta_c \approx 122^\circ$ based on data reported in Ref. [39].

The results of simulations are shown in Fig. 8. For short annealing times the film swiftly withdraws from the pit and its outer surface is flattened. Later on the film surface at the outer edges of the simulation cell touches the substrate, which in terms of periodic arrangement of simulation cells means that the film breaks down into isolated particles. With increasing annealing time, the pore begins to shrink, and the particle sinks to the bottom of the pit. We have clearly observed the film flattening and its withdrawal from the sharp pits in our experiments (see Fig. 4c, 5). Whether or not the film will break down into individual particles depends on a combination of several parameters, such as film thickness, geometry of the pits and their mutual arrangement, diffusion coefficients, and the contact angle. It is well possible that the breakdown of the film is prevented for large film patches under present experimental conditions, resulting in film flattening and its withdrawal from the pits, and some stabilization of the flattened film. Another reason for the stabilization of the flattened film may be the grain growth in the film: when no GBs connected the pore with the outer surface are left, the flattened film morphology becomes “frozen”.

4.2.2. Slow-down of dewetting holes expansion by surface steps

A remarkable feature of observed DW behavior of Au film on the surface of oxidized Ti-6Al-4V alloy is a stabilization of nanoporous, partially dewetted film for long annealing times and high temperatures (see Fig. 6). This is highly surprising, taking into account that the natural surface roughness actually promotes the nucleation of dewetting holes at the early stages of DW. At the advanced stages of DW, however, the nanoporous film preserves its continuity even after annealing at 500 °C for 2 h. We propose that this stabilization of partially dewetted film is related to the pinning of the film-substrate triple lines by sharp asperities and steps on the rough surface. Such pinning is well-known in wetting of rough surfaces by liquids, and it causes significant hysteresis of the wetting angle [40]. To the best of our knowledge, this triple line pinning has not been considered in the case of solid-state DW. For illustration, we will consider the edge of the dewetting hole in the vicinity of a surface step in a geometry in which the direction of the film edge retraction points towards the lower terrace. In or-

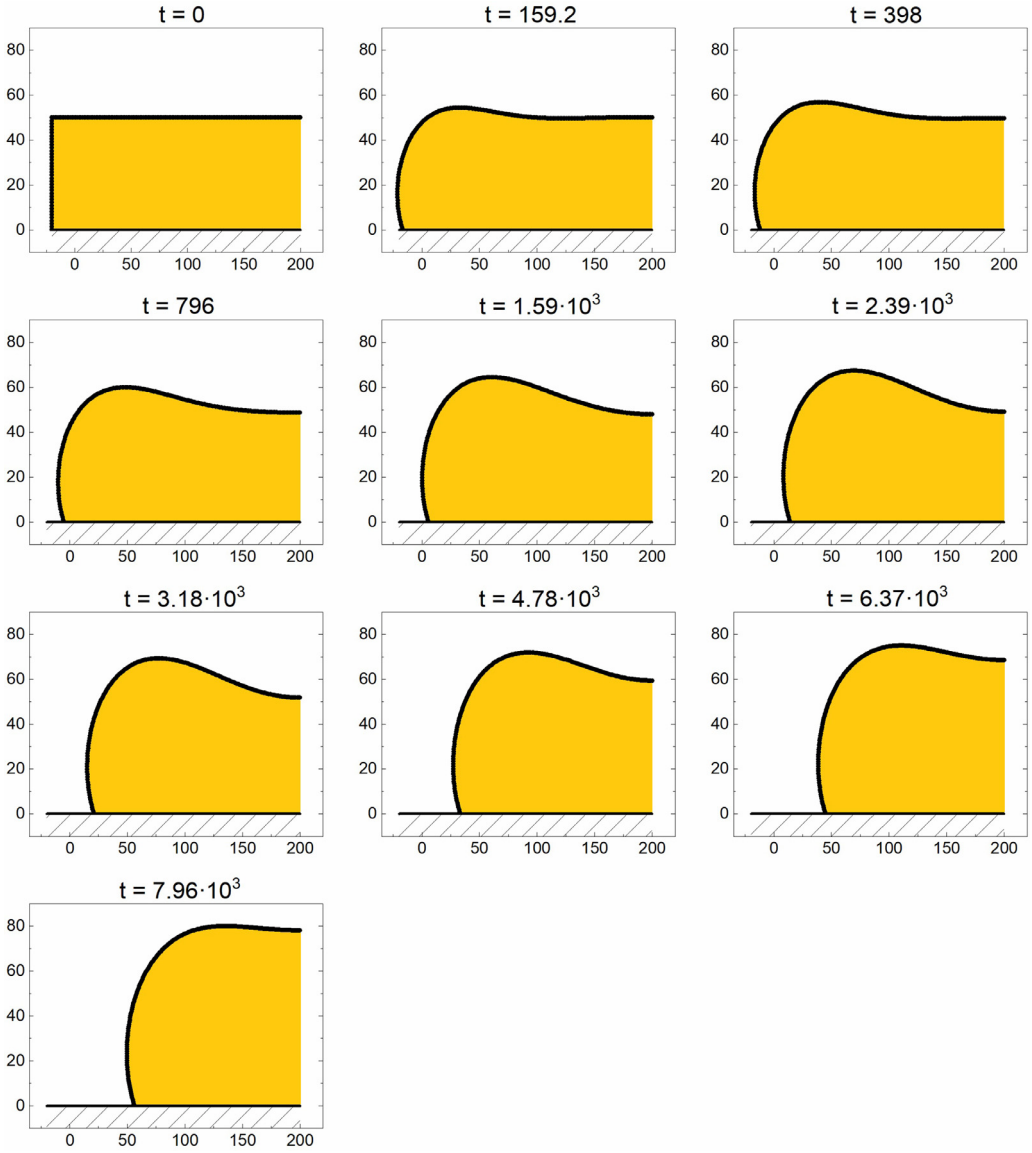

Fig. 10. A cross-section showing evolution of the film deposited on a flat substrate over time (t, s); dimensions are in units of nm.

der to avoid the singularities in simulations, we will approximate a sharp step by a continuous function:

$$y = -\frac{5}{\pi}\arctan\left(\frac{x}{0.5}\right), \tag{3}$$

where x and y are given in nm. The Eq. (3) describes a step of 5 nm in height centered around $x = 0$. The calculated morphologies of receding film edge after different annealing times are given in Fig. 9. Again, the zero-flux boundary conditions were employed in simulations. It can be clearly seen that the receding edge is pinned by a surface step, followed by a decrease of apparent contact angle. In comparison, annealing of the thin film of the same thickness deposited on the flat surface results in the film retraction typical for the DW process (Fig. 10). During the maximum simulated time of 7960 s, the edge of the film on a flat substrate retracts by more than 50 nm. This distance is insignificantly affected by the employed zero-flux boundary condition, which was verified by performing simulation in a wider cell (320 nm). During the same time, the edge of the film above the substrate step barely changes its position. These illustrative simulations demonstrate that the sharp topography features on a surface with random natural roughness can stop the expansion of DW holes and stabilize the porous continuous film. It should be emphasized that the main factor responsible for the film edge pinning is the step sharpness as given by the Eq. (3), and not the overall step amplitude. Thus, similar pinning should be caused by a sharp asperity or by the edge of cuboidal Ti oxide grain.

A final comment is due here. We claim that stabilization of the porous film structure is most efficient when the average distance between the sharp edges of oxide cuboids is of the same order of magnitude as the initial film thickness. Fig. 7 demonstrates that for much thinner films the DW on oxide grain facets will proceed similarly to the DW on flat substrates, resulting in small isolated metal particles dotting the oxide crystals. For the much thicker film, the rough substrate can be treated as a heterogeneous surface characterized by a contact angle given by Cassie-Baxter law, which is different from the contact angle of Au on a flat Ti oxide substrate [41]. In this case the DW will result in large isolated Au particles covering many rutile grains. The distribution of the distances between neighboring edges of Ti oxide grains of the as-oxidized Ti-6Al-4V alloy is shown in Fig. S6 of *Supplementary Material*. The average distance is 67 nm, comparable to the thickness of the as-deposited Au film of 50 nm. This is why in the present work the oxidized

alloy was so efficient in stabilizing complex porous morphology of partially dewetted Au film.

5. Conclusions

We have studied the solid-state dewetting of 50 nm-thick Au film deposited on oxidized surfaces of biomedical Ti-6Al-4V alloy initially processed by mechanical grinding. The following conclusions can be drawn from this study:

1. The thickness of the crystalline TiO_2 layer for the oxidized alloy is about 900 nm. The oxide is mainly composed of rutile phase, with some enrichment in alumina in the topmost layer of the grown oxide. The surface of the oxidized alloy consists of cuboidal oxide grains that form a very rough surface with characteristic random prismatic pits.
2. The 50 nm-thick Au film deposited on the oxidized alloy was polycrystalline and exhibited thickness inhomogeneities. Nevertheless, most sharp pits on the surface of oxidized alloy were conformally filled with Au.
3. Short annealings (5–25 min) at the temperature of 300 °C resulted in formation of holes in the Au film. Holes formed in the vicinity of surface topography features such as hills or steps. Surprisingly, the area density of holes was higher than in the case of thinner Au film (20 nm) deposited on flat crystalline TiO_2 substrate and annealed at higher temperature (400 °C).
4. The early dewetting stages of the Au film on oxidized alloy were accompanied by Au film flattening and its withdrawal from the sharp surface pits.
5. At the late dewetting stages highly porous, but continuous Au film on the oxidized sample was stabilized, and isolated islands and particles did not form.
6. We performed a series of numerical simulations of the Au film topography evolution based on curvature-driven surface diffusion. We demonstrated that taking into account the GB diffusion is essential for describing the kinetics of film flattening and its withdrawal from prismatic pits. Stabilization of the porous film at the late stages of dewetting was attributed to the pinning of the triple lines by the surface steps and other sharp surface features, thus slowing down the expansion of dewetting holes.

Finally, the nanoporous continuous Au coating obtained at the late stages of dewetting may be interesting from the biomedical point of view since it enables combining Au functionalization with the drug storage in the film pores, followed by controlled drug release. Moreover, one should not be constrained by Ag and Au coatings for surface biofunctionalization. We believe that other metals widely employed in biomedicine, such as magnesium, iron, and zinc, could also be employed for implant surface modification by solid-state dewetting of respective coatings.

Declaration of Competing Interest

The authors declare that they have no known competing financial interests or personal relationships that could have appeared to influence the work reported in this paper.

Acknowledgments

This work was supported by the Ministry of Science & Technology of Israel (grant 3-16534) and Russian Foundation for Basic Research (grant 19-58-06002). The thin films deposition was performed in the Technion Micro-nano Fabrication and Printing Unit (MNFPU).

Supplementary materials

Supplementary material associated with this article can be found, in the online version, at doi:10.1016/j.actamat.2022.117919.

References

[1] C. Stewart, B. Akhavan, S.G. Wise, M.M.M. Bilek, A review of biomimetic surface functionalization for bone-integrating orthopedic implants: mechanisms, current approaches, and future directions, Prog. Mater. Sci. 106 (2019) 100588, doi:10.1016/j.pmatsci.2019.100588.
[2] J. Li, X. Cui, G.J. Hooper, K.S. Lim, T.B.F. Woodfield, Rational design, bio-functionalization and biological performance of hybrid additive manufactured titanium implants for orthopaedic applications: a review, J. Mech. Behav. Biomed. Mater. 105 (2020) 103671, doi:10.1016/j.jmbbm.2020.103671.
[3] S. Qian, Y. Qiao, X. Liu, Selective biofunctional modification of titanium implants for osteogenic and antibacterial applications, J. Mater. Chem. B. 2 (2014) 7475–7487, doi:10.1039/c4tb00973h.
[4] T. Cohen-Karni, K.J. Jeong, J.H. Tsui, G. Reznor, M. Mustata, M. Wanunu, A. Graham, C. Marks, D.C. Bell, R. Langer, D.S. Kohane, Nanocomposite gold-silk nanofibers, Nano Lett 12 (2012) 5403–5406, doi:10.1021/nl302810c.
[5] X. Zheng, J. Sun, W. Li, B. Dong, Y. Song, W. Xu, Y. Zhou, L. Wang, Engineering nanotubular titania with gold nanoparticles for antibiofilm enhancement and soft tissue healing promotion, J. Electroanal. Chem. 871 (2020) 114362, doi:10.1016/j.jelechem.2020.114362.
[6] D.N. Heo, W.K. Ko, H.R. Lee, S.J. Lee, D. Lee, S.H. Um, J.H. Lee, Y.H. Woo, L.G. Zhang, D.W. Lee, I.K. Kwon, Titanium dental implants surface-immobilized with gold nanoparticles as osteoinductive agents for rapid osseointegration, J. Colloid Interface Sci. 469 (2016) 129–137, doi:10.1016/j.jcis.2016.02.022.
[7] D. Merker, B. Popova, T. Bergfeldt, T. Weingärtner, G.H. Braus, J.P. Reithmaier, C. Popov, Antimicrobial propensity of ultrananocrystalline diamond films with embedded silver nanodroplets, Diam. Relat. Mater. 93 (2019) 168–178, doi:10.1016/j.diamond.2019.02.003.
[8] P. Hajdu, S. Biri, A. Cs, T. Ferenc, Optimized size and distribution of silver nanoparticles on the surface of titanium implant regarding cell viability, Appl. Sci. 10 (2020) 1–13 https://doi.org/doi:10.3390/app10207063.
[9] S. Madeira, A. Barbosa, C.G. Moura, M. Buciumeanu, F.S. Silva, O. Carvalho, Aunps and Agμps-functionalized zirconia surfaces by hybrid laser technology for dental implants, Ceram. Int. 46 (2020) 7109–7121, doi:10.1016/j.ceramint.2019.11.203.
[10] Y. Kojima, T. Kato, Nanoparticle formation in Au thin films by electron-beam-induced dewetting, Nanotechnology 19 (2008), doi:10.1088/0957-4484/19/25/255605.
[11] D. Kim, A.L. Giermann, C.V. Thompson, Solid-state dewetting of patterned thin films, Appl. Phys. Lett. 95 (2009) 2009–2011, doi:10.1063/1.3268477.
[12] D. Amram, E. Rabkin, Core(Fe)-shell(Au) nanoparticles obtained from thin Fe/Au bilayers employing surface segregation, ACS Nano 8 (2014) 10687–10693, doi:10.1021/nn504284d.
[13] A.G. Harvey, E.W. Hill, A. Bayat, Designing implant surface topography for improved biocompatibility, Expert Rev. Med. Devices. 10 (2013) 257–267, doi:10.1586/erd.12.82.
[14] M. Ribeiro, F.J. Monteiro, M.P. Ferraz, Infection of orthopedic implants with emphasis on bacterial adhesion process and techniques used in studying bacterial-material interactions, Biomatter 2 (2012) 176–194, doi:10.4161/biom.22905.
[15] D. Wang, R. Ji, P. Schaaf, Formation of precise 2D Au particle arrays via thermally induced dewetting on pre-patterned substrates, Beilstein J. Nanotechnol. 237 (2) (2011) 318–326, doi:10.3762/BJNANO.2.37.
[16] A.L. Giermann, C.V. Thompson, Three-dimensional graphoepitaxial alignment resulting from solid-state dewetting of Au films on surfaces with monoperiodic topography, Appl. Phys. Lett. (2012) 101, doi:10.1063/1.4740277.
[17] A.L. Giermann, C.V. Thompson, Requirements for graphoepitaxial alignment through solid-state dewetting of Au films, J. Appl. Phys. 109 (2011), doi:10.1063/1.3567302.
[18] A.L. Giermann, C.V. Thompson, Solid-state dewetting for ordered arrays of crystallographically oriented metal particles, Appl. Phys. Lett. 86 (2005) 1–3, doi:10.1063/1.1885180.
[19] Y.J. Oh, C.A. Ross, Y.S. Jung, Y. Wang, C.V. Thompson, Cobalt nanoparticle arrays made by templated solid-state dewetting, Small 5 (2009) 860–865, doi:10.1002/smll.200801433.
[20] W. Jiang, Y. Wang, D.J. Srolovitz, W. Bao, Solid-state dewetting on curved substrates, Phys. Rev. Mater. 2 (2018) 1–13, doi:10.1103/PhysRevMaterials.2.113401.
[21] GOST 19807-91, Wrought titanium and titanium alloys, Grades (1991).
[22] E. Gemelli, N.H.A. Camargo, Oxidation kinetics of commercially pure titanium, Matéria (Rio Janeiro) 12 (2007) 525–531, doi:10.1590/s1517-70762007000300014.
[23] S. Tkachenko, O. Datskevich, K. Dvořák, Z. Spotz, L. Kulak, L. Čelko, Isothermal oxidation behavior of experimental Ti–Al–Si alloys at 700°C in air, J. Alloys Compd. 694 (2017) 1098–1108, doi:10.1016/j.jallcom.2016.10.044.
[24] H.L. Du, P.K. Datta, D.B. Lewis, J.S. Burnell-Gray, Air oxidation behaviour of Ti6Al4V alloy between 650 and 850°, Corros. Sci. 36 (1994) 631–642, doi:10.1016/0010-938X(94)90069-8.
[25] S. Frangini, A. Mignone, F. de Riccardis, Various aspects of the air oxidation behaviour of a Ti6Al4V alloy at temperatures in the range 600-700°C, J. Mater. Sci. 29 (1994) 714–720, doi:10.1007/BF00445984.

[26] H. Sadan, W.D. Kaplan, Au-Sapphire (0001) solid-solid interfacial energy, J. Mater. Sci. 41 (2006) 5099–5107, doi:10.1007/s10853-006-0437-5.
[27] F. Cosandey, Epitaxy, interfacial energy and atomic structure of Au/TiO2 interfaces, Philos. Mag. 93 (2013) 1197–1218, doi:10.1080/14786435.2013.770178.
[28] M. Sriubas, V. Kavaliūnas, K. Bočkutė, P. Palevičius, M. Kaminskas, Ž. Rinkevičius, M. Ragulskis, G. Laukaitis, Formation of Au nanostructures on the surfaces of annealed TiO2 thin films, Surfaces and Interfaces 25 (2021) 101239, doi:10.1016/j.surfin.2021.101239.
[29] P.D. Nsimama, A. Herz, D. Wang, P. Schaaf, Influence of the substrate on the morphological evolution of gold thin films during solid-state dewetting, Appl. Surf. Sci. 388 (2016) 475–482, doi:10.1016/j.apsusc.2015.11.185.
[30] C.M. Müller, R. Spolenak, Microstructure evolution during dewetting in thin Au films, Acta Mater 58 (2010) 6035–6045, doi:10.1016/j.actamat.2010.07.021.
[31] J.Y. Kwon, T.S. Yoon, K.B. Kim, S.H. Min, Comparison of the agglomeration behavior of Au and Cu films sputter deposited on silicon dioxide, J. Appl. Phys. 93 (2003) 3270–3278, doi:10.1063/1.1556178.
[32] A. Kosinova, O. Kovalenko, L. Klinger, E. Rabkin, Mechanisms of solid-state dewetting of thin Au films in different annealing atmospheres, Acta Mater 83 (2015) 91–101, doi:10.1016/j.actamat.2014.09.049.
[33] R. Wenzel, Resistance of solid surfaces to wetting by water, Ind. Eng. Chem. 28 (1937) 988–994, doi:10.1017/cbo9781316146743.
[34] E. Dornel, J.C. Barbé, F. De Crécy, G. Lacolle, J. Eymery, Surface diffusion dewetting of thin solid films: Numerical method and application to Si/SiO2, Phys. Rev. B - Condens. Matter Mater. Phys. 73 (2006) 1–10, doi:10.1103/PhysRevB.73.115427.
[35] H. Göbel, P. von Blanckenhagen, A study of surface diffusion on gold with an atomic force microscope, Surf. Sci. 331–333 (1995) 885–890, doi:10.1016/0039-6028(95)00206-5.
[36] J.W. Martin, R.D. Doherty, B. Cantor, Stability of Microstructure in Metallic Systems, Cambridge University Press, 1997, doi:10.1017/CBO9780511623134.
[37] N.A. Gjostein, Surface Self-Diffusion, in: Met. Surfaces Struct. Energ. Kinet, American Society for Metals, Ohio, 1963, pp. 99–154.
[38] D. Gupta, Grain-boundary self-diffusion in Au by Ar sputtering technique, J. Appl. Phys. 44 (1973) 4455–4458, doi:10.1063/1.1661981.
[39] D. Chatain, F. Chabert, V. Ghetta, J. Fouletier, New experimental setup for wettability characterization under monitored oxygen activity: I, role of oxidation state and defect concentration on oxide wettability by gold, J. Am. Ceram. Soc. 76 (1993) 1568–1576, doi:10.1111/j.1151-2916.1993.tb03941.x.
[40] P.-G. de Gennes, F. Brochard-Wyart, D. Quéré, Special Interfaces, Capillarity Wetting Phenom (2004) 215–259.
[41] D. Bonn, J. Eggers, J. Indekeu, J. Meunier, Wetting and spreading, Rev. Mod. Phys. 81 (2009) 739–805, doi:10.1103/REVMODPHYS.81.739/FIGURES/55/MEDIUM.